Matter

CellPress

Article

Enhanced ionic conductivity and lack of paddle-wheel effect in pseudohalogen-substituted Li argyrodites

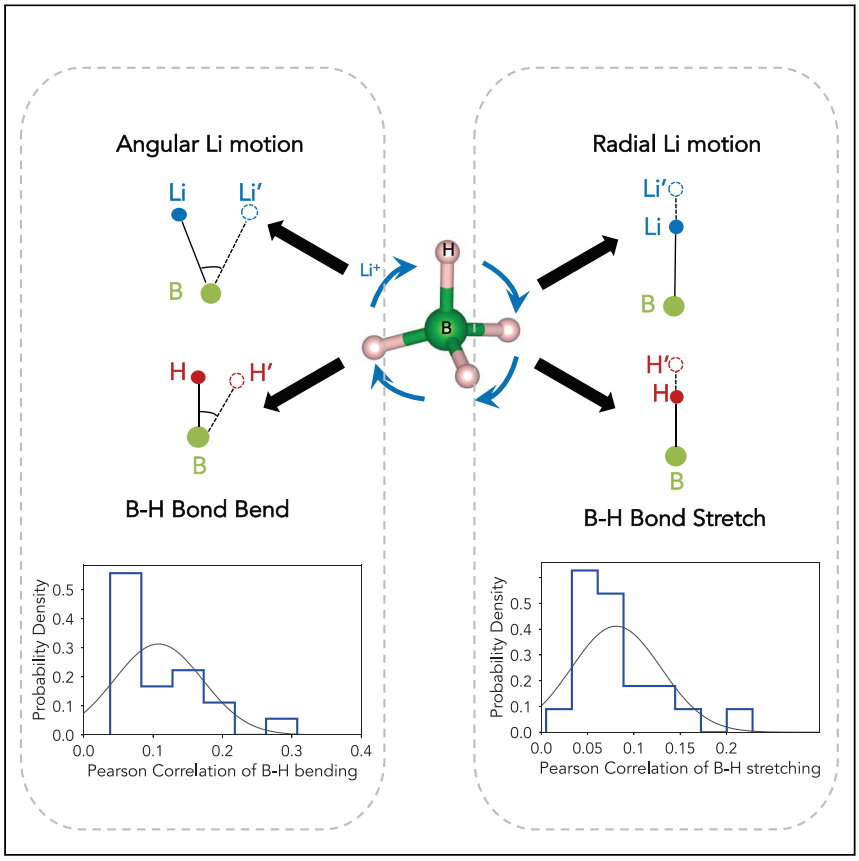

Superionic conductors are important for all-solid-state batteries. In this work, we demonstrate the capability of improving ionic conductivity using cluster ions through a case study on the pseudohalogen-substituted Li argyrodite. Simulations and experiments are combined to provide a mechanistic understanding of the cluster-ion effect on conductivity.

Yingzhi Sun, Bin Ouyang, Yan Wang, ..., Valentina Lacivita, Yinsheng Guo, Gerbrand Ceder

gceder@berkeley.edu

Highlights

BH_4-substituted Li argyrodite with enhanced conductivity is synthesized

A paddle-wheel mechanism is not found in BH_4-substituted Li argyrodite

Enhanced conductivity originates from the weak interaction between Li and BH_4

Cluster-ion substitution is proven to be a strategy to engineer ionic conductivity

3 **Understanding**
Dependency and conditional studies on material behavior

Sun et al., Matter 5, 1–17
December 7, 2022
https://doi.org/10.1016/j.matt.2022.08.029

Please cite this article in press as: Sun et al., Enhanced ionic conductivity and lack of paddle-wheel effect in pseudohalogen-substituted Li argyrodites, Matter (2022), https://doi.org/10.1016/j.matt.2022.08.029

Matter

CellPress

Article

Enhanced ionic conductivity and lack of paddle-wheel effect in pseudohalogen-substituted Li argyrodites

Yingzhi Sun,[1,2,6] Bin Ouyang,[1,2,3,6] Yan Wang,[4] Yaqian Zhang,[2] Shuo Sun,[5] Zijian Cai,[1,2] Valentina Lacivita,[4] Yinsheng Guo,[5] and Gerbrand Ceder[1,2,7,*]

SUMMARY

Superionic conductors are key to the development of safe and high-energy-density, all-solid-state batteries. Using a combined theoretical and experimental approach, we explore the feasibility of increasing the ionic conductivity through pseudohalogen substitution in the Li argyrodite structure. Under the guidance of calculated thermodynamic stability, BH_4-substituted Li argyrodite, $Li_{5.91}PS_{4.91}(BH_4)_{1.09}$, was successfully synthesized via a mechanochemical method. As-synthesized BH_4-substituted Li argyrodite displays an ionic conductivity of 4.8 mS/cm at 25°C. *Ab initio* molecular dynamics simulation trajectory analysis was used to investigate how BH_4 facilitates Li-ion diffusion and indicates only a weak correlation with the B–H bond motion. We find that the enhanced conductivity mainly originates from the weak interaction between Li and BH_4 and find no evidence of a paddle-wheel effect from the polyanion. This work provides insight into how cluster ions enhance Li diffusion and systematically describes how to explore superionic conductors with pseudohalogen substitution.

INTRODUCTION

The application of solid-state electrolytes provides opportunities for batteries that are safer and more powerful than current state-of-the-art Li-ion batteries.[1,2] Driven by the demand for solid-state electrolytes, there has been a rapidly growing interest in the discovery of solid-state alkali ionic conductors with ionic conductivities equal to or higher than those of liquid electrolytes.[3–9]

While most recent work for improving ionic conductivity has focused on substituting cation sites,[9–12] less work has been done on modifying the anion chemistry, although the anion framework is known to be important for ionic conductivity.[8] In this paper we focus on cluster-ion substitution, as it provides an option for engineering the anion framework. Compared with single-ion substitution, cluster-ion substitution provides more degrees of freedom, including bond stretching and bond bending, which may help the alkali-metal to preserve their coordination as much as possible as they migrate through the transition state, a factor that is important in the migration of many cations.[8,13] To date, it remains unclear whether and how these additional degrees of freedom lead to higher conductivity, even though high conductivities have been reported in several recent studies.[14–19] Specifically, several orders of magnitude enhancement in the ionic conductivity has been reported in both theoretical and experimental work applying cluster-ion substitution in antiperovskite-type materials.[17–19] The cluster ions used in those reports can be classified as

PROGRESS AND POTENTIAL

Substituting a single ion site with a cluster ion is considered a promising approach to increase the ionic conductivity of fast Li-ion conductors. However, it remains unclear how cluster ions can promote Li diffusion. In this work, using a combined theoretical and experimental approach, we explore the possibility of enhancing ionic conductivity through pseudohalogen substitution in the Li argyrodite structure. BH_4-substituted Li argyrodite is successfully synthesized and displays an enhanced ionic conductivity. We further demonstrate that the enhanced conductivity mainly originates from the weak interaction between Li and BH_4 polyanion instead of the typically expected paddle-wheel effect rising from cluster-ion rotation. The results here provide a mechanistic understanding of how cluster ions can help increase Li-ion conductivity and shed light on design strategies for pseudohalogen-substituted fast Li-ion conductors.

pseudohalogen anions, as the formal charge of such cluster ions equals that of a halogen, and the strong covalent interactions within such a cluster ion cause it to behave as a unit. Considering the frequent appearance of halogens in fast ionic conductors, it is important to understand how pseudohalogen substitution influences ionic conductivity.

The argyrodite structure is a good framework to study the pseudohalogen effect, as it already has reasonable conductivity with the presence of regular halogens.[4,20–23] As the halogen site in argyrodite has only mobile Li^+ in its first coordination shell, it is loosely bonded with the rest of the framework, creating the expectation that it may be easier to substitute.[3,24] The most widely studied argyrodites are derived from halogen substitution in the Li_7PS_6 argyrodite prototype, which yields various forms of Li_6PS_5Cl, Li_6PS_5Br, and Li_6PS_5I. Halogen substitution has been reported to have a beneficial effect on the diffusion of Li ions, with the ionic conductivity of halogen-substituted argyrodite-type materials varying from 10^{-3} to 10 mS/cm.[4,24–29]

In this paper, we explore the feasibility of enhancing the ionic conductivity through pseudohalogen substitution in the Li-argyrodite system using a combined theoretical and experimental approach, including first-principles stability analysis, solid-state synthesis, structure characterization, and *ab initio* molecular dynamic (AIMD) analysis. A computational screening of potential Li-argyrodite pseudohalides to determine the synthetically accessible argyrodite pseudohalides points at BH_4-substituted Li argyrodites as the most stable pseudohalides. An argyrodite-type material with the composition $Li_{5.91}PS_{4.91}(BH_4)_{1.09}$ was successfully synthesized using a mechanochemical method and shown to have a high ionic conductivity of 4.8 mS/cm at RT, considerably higher than that of conventional halogen-substituted Li argyrodites.

When explaining the effect of polyanions/cluster anions on Li-ion diffusion, most recent work has centered on whether there is a synergistic effect between the polyanions and Li diffusion (the so-called "paddle-wheel" effect).[16,19,30–32] Our theoretical analysis shows that the motion of Li ions has only a weak relationship with any motion of the BH_4 anion. Hence, rather than appealing to a paddle-wheel effect, we argue that the enhanced conductivity mainly originates from the Li-pseudohalogen interaction, which is weaker than the Li-halogen (Cl, etc.) interaction. As a result, Li ions are trapped for a shorter time near the pseudohalide groups and diffuse faster. This finding also indicates that the origin of higher conductivity in the argyrodite structure with pseudohalogen substitution is the flattening of the energy landscape with the introduction of light and highly covalent cluster ions, rather than any "dynamical coupling" between Li diffusion and polyanion rotation, as has been speculated in the literature. Our study provides a mechanistic understanding of how pseudohalogen substitution can help increase Li-ion conductivity, shedding light on design strategies for optimizing ionic conductivity by engineering the anion framework of conductors.

RESULTS

Crystal structure and phase stability

The general (pseudo)halogen-substituted argyrodite is reported to have a crystal structure with cubic symmetry as shown in Figure 1A. Three crystallographic positions in the argyrodite structure, 4a, 4c, and 16e, are associated with sulfur ions. The 4b site is occupied by P, which binds four S ions to it into a PS_4 group. In contrast, the 4a and 4c sites are occupied by S atoms that are relatively far away from all other

[1]Department of Materials Science and Engineering, University of California, Berkeley, Berkeley, CA 94720, USA

[2]Materials Sciences Division, Lawrence Berkeley National Laboratory, Berkeley, CA 94720, USA

[3]Department of Chemistry and Biochemistry, Florida State University, Tallahassee, FL 32306, USA

[4]Advanced Materials Lab, Samsung Advanced Institute of Technology–America, Samsung Semiconductor, Inc., Cambridge, MA 02138, USA

[5]Department of Chemistry, University of Nebraska–Lincoln, Lincoln, NE 68526, USA

[6]These authors contributed equally

[7]Lead contact

*Correspondence: gceder@berkeley.edu

https://doi.org/10.1016/j.matt.2022.08.029

Please cite this article in press as: Sun et al., Enhanced ionic conductivity and lack of paddle-wheel effect in pseudohalogen-substituted Li argyrodites, Matter (2022), https://doi.org/10.1016/j.matt.2022.08.029

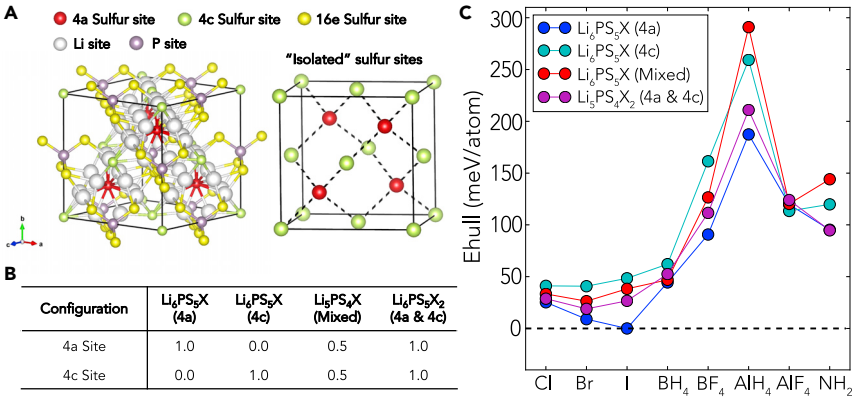

B

Configuration	Li_6PS_5X (4a)	Li_6PS_5X (4c)	Li_5PS_4X (Mixed)	$Li_6PS_5X_2$ (4a & 4c)
4a Site	1.0	0.0	0.5	1.0
4c Site	0.0	1.0	0.5	1.0

Figure 1. Structure and stability of Li argyrodites

(A) General structure of argyrodite with different sulfur sites distinguished by colors (4a with red, 4c with green, and 16e with yellow).

(B) Sulfur site occupancies for four types of substitution.

(C) Energy above the hull (E_{hull}) of Li argyrodites with different substitutions.

non-Li atoms (>4 Å) and are not considered to be part of a covalent bond complex. As a result, sulfur in the 4a and 4c sites is usually easier to substitute.[25]

To understand the compositional range over which different Li-argyrodite pseudohalides can exist, five pseudohalide ions were considered for substitution on 4a and/or 4c. Four types of substitution were considered, distinguished by their site occupancy (shown in Figure 1B). The first three types of substitution form Li_6PS_5X (X = halogen or pseudohalogen), which corresponds to the occupancy of a (pseudo)halogen on either the 4a or the 4c site, or half-occupancy on both the 4a and the 4c sites. In the fourth type, both the 4a and the 4c sites are fully substituted by the (pseudo)halogen, leading to the composition $Li_5PS_4X_2$ (X = halogen or pseudohalogen). To evaluate the energy of these compounds, we enumerated the 10 possible Li arrangements across the 48h sites (denoted as the Li sites) and picked the one with lowest density functional theory (DFT) energy. We did not consider possible occupancy of Li in other sites, such as 48h′, 16e, and 24g, because we found that the change in energy of our structures when moving a Li from 48h to 48h′ is small (see Table S1), and will therefore not significantly influence relative phase stability; but including it in all calculations would require unnecessarily large supercells. For each Li-Vacancy (Li-Vac) configuration on the 48 h sites, the S-(pseudo)halogen ordering with lowest electrostatic energy was selected for DFT calculations. The orientation of the pseudohalogen was initialized by rotating the pseudohalogen until the average interatomic distance between the cluster ions and the neighboring cations was maximized. The phase stability was evaluated by comparing the energy of the substituted argyrodites with that of all the possible combinations of competing phases (the convex hull construction).[33] Figure 1C shows that most argyrodites have non-zero energy above the convex hull (E_{hull}), indicating that at 0 K, they are not a thermodynamic ground state. However, the halide versions of the argyrodites, such as Li_6PS_5Cl and Li_6PS_5Br, have been synthesized,[3] indicating that they can be stabilized by entropy, as is the case for other fast ion conductors,[34,35] or that metastable synthesis pathways to their formation exist.[36] It should be mentioned that we use the E_{hull} values only to indicate the relative stability of argyrodites with different (pseudo)halogen substitutions. An argyrodite with a low E_{hull} value does not necessarily guarantee synthetic accessibility. To give an example, $Li_5PS_4X_2$ (X = Cl, Br, I) has never been reported experimentally in the literature. This is

Please cite this article in press as: Sun et al., Enhanced ionic conductivity and lack of paddle-wheel effect in pseudohalogen-substituted Li argyrodites, Matter (2022), https://doi.org/10.1016/j.matt.2022.08.029

Table 1. Competing phases for BH_4 substitution and halide substitution

Materials	Competing phases	Materials	Competing phases
$Li_6PS_5BH_4$	$LiSH + Li_2S + BP$	Li_6PS_5X (X = Cl, Br, I)	$Li_3PS_4 + Li_2S + LiX$
$Li_5PS_4(BH_4)_2$	$LiBH_4 + LiSH + BP$	$Li_5PS_4X_2$ (X = Cl, Br, I)	$Li_3PS_4 + Li_2S + LiX$

consistent with a broad analysis of metastable compounds, which indicates that, while low E_{hull} is required for the possible existence of metastable compounds, it is not a sufficient condition.[36]

The phases that compete for phase stability for each argyrodite are given in Table 1. Most of these are stoichiometric phases, implying that they will not generate much configurational entropy at non-zero temperature and, hence, will create more favorable conditions for the formation of the argyrodite at higher temperature.

Synthesis and characterization

Our *ab initio* results indicate that BH_4-substituted argyrodites have the lowest E_{hull} among the pseudohalogen-substituted compounds, making them likely candidates for synthesis. In addition, Sakuda et al. recently reported that an argyrodite phase appeared in the $(100 - x)(0.75Li_2S \cdot 0.25P_2S_5) \cdot xLiBH_4$ mixture with $x \geq 43$.[37] So, we set BH_4-substituted argyrodites as our target materials. β-Li_3PS_4, which is a metastable phase at RT, was used as the precursor to increase the thermodynamic driving force for the formation reaction of the pseudohalide argyrodite. In addition, the Li_3PS_4 precursor has the PS_4 groups preformed, which may make it easier to form the argyrodite. Because $LiBH_4$ decomposes at high temperature,[38] a heating process is not suitable for this reaction. Instead, a mechanochemical method using high-energy ball milling (SpexSamplePrep 8000M mixer/mill, 1,425 rpm) was used. To prevent the sample temperature from becoming too high, the ball milling was interrupted for 15 min after every 30 min milling. In addition, we find that excess $LiBH_4$ is necessary to the synthesis of BH_4-substituted argyrodite since $LiBH_4$ is easily oxidized and consumed during the synthesis. When the precursors were mixed in the stoichiometric ratio of $Li_6PS_5BH_4$ (β-Li_3PS_4:$LiBH_4$:Li_2S = 1:1:1), no argyrodite phase was formed in the product (Figure S1).

Synchrotron X-ray diffraction (XRD) (shown in Figure 2A) was conducted to confirm that an argyrodite phase was formed with a small amount (~2.8 wt %) of remaining $LiBH_4$. The synchrotron XRD pattern was refined using the Rietveld method with the TOPAS v.6 software package to determine the lattice parameters, atomic positions, and occupancies. The best fits were obtained when the BH_4^- and S^{2-} ions are assumed to be disordered over the 4a site and 4c site. As shown in Table 2, the refined B occupancies of the 4a and 4c sites are 0.584 and 0.506, respectively, indicating that the chemical formula of the as-synthesized BH_4-substituted argyrodite is $Li_{5.91}PS_{4.91}(BH_4)_{1.09}$.

Transmission electron microscopy (TEM) electron diffraction (ED) patterns of the as-synthesized materials are presented in Figure 2B. The diffraction spots match with the calculated diffraction rings of the argyrodite structure, confirming the formation of the argyrodite phase. Scanning transmission electron microscopy (STEM) energy dispersive spectroscopy (EDS) mapping images are presented in Figure 2C and indicate a homogeneous distribution of B throughout the particles, further corroborating the bulk substitution of BH_4.

Please cite this article in press as: Sun et al., Enhanced ionic conductivity and lack of paddle-wheel effect in pseudohalogen-substituted Li argyrodites, Matter (2022), https://doi.org/10.1016/j.matt.2022.08.029

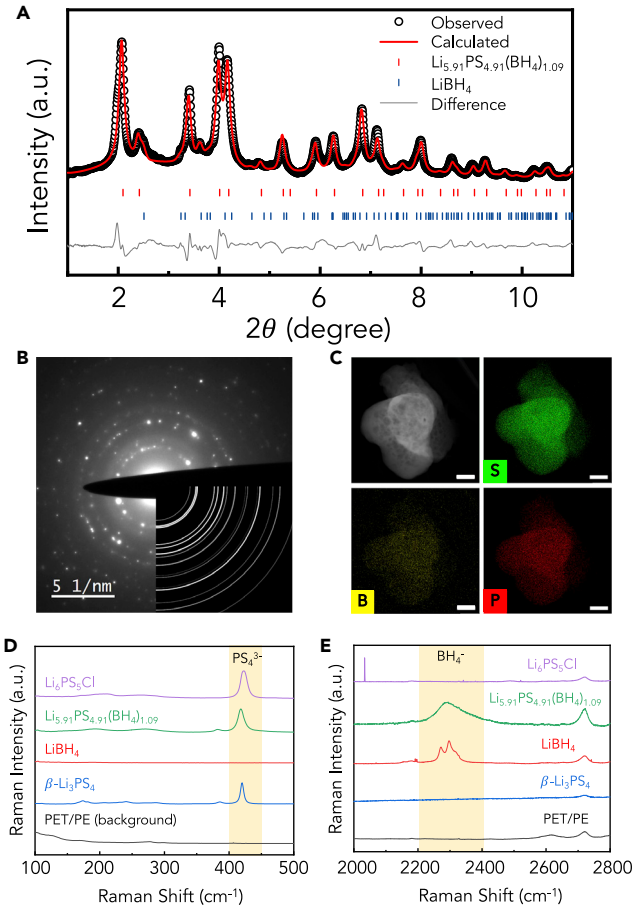

Figure 2. Characterization of as-synthesized BH_4-argyrodite

(A) Synchrotron XRD pattern of as-synthesized BH_4-argyrodite.

(B) Electron diffraction pattern of as-synthesized BH_4-argyrodite. Calculated diffraction rings of the argyrodite structure are shown in the bottom right corner.

(C) STEM-EDS mapping of the element distribution in a representative particle cluster of the BH_4-argyrodite (scale bar: 100 nm).

(D and E) Raman spectra of Li_6PS_5Cl, $Li_{5.91}PS_{4.91}(BH_4)_{1.09}$, $LiBH_4$, β-Li_3PS_4, and polyethylene terephthalate(PET)/polyethylene(PE) (background) in the 100 to 500 cm^{-1} region and 2,000 to 2,800 cm^{-1} region, respectively.

To confirm the successful incorporation of the BH_4^- unit, we also measured the Raman response of the argyrodite electrolytes and their precursors. The BH_4^- internal stretching modes have characteristic frequencies residing in the 2,200 to 2,400 cm^{-1} region, allowing for easy and unambiguous identification. As shown in Figure 2E, we observed the BH_4^- stretching modes in the $Li_{5.91}PS_{4.91}(BH_4)_{1.09}$ sample and in the $LiBH_4$ positive control compound, whereas in the β-Li_3PS_4 and Li_6PS_5Cl negative control compounds, the BH_4^- stretching region is spectrally silent. The presence of the BH_4^- stretching modes provides further evidence that the BH_4^- is successfully incorporated into the argyrodite electrolyte.

Electrochemical performance

Electrochemical impedance spectroscopy (EIS) measurements were performed to determine the ionic conductivity of the cold-pressed $Li_{5.91}PS_{4.91}(BH_4)_{1.09}$, with the results shown in Figures 3A and 3B. The impedance data were fit with an equivalent circuit consisting of one parallel constant phase element (CPE)/resistor in series with

Please cite this article in press as: Sun et al., Enhanced ionic conductivity and lack of paddle-wheel effect in pseudohalogen-substituted Li argyrodites, Matter (2022), https://doi.org/10.1016/j.matt.2022.08.029

Table 2. Atomic site information for BH_4-substituted Li argyrodite based on Rietveld refinement of synchrotron XRD data

Atom	Wyckoff position	x	y	z	B_{iso}/ Å^2	Site occupancy
Li1	48h	0.3053(2)	0.3053(2)	0.0024(8)	4	0.334(4)
Li2	24g	0.75	0.0386(4)	0.25	4	0.315(9)
B1	4a	0	0	0	4.2(4)	0.584(8)
S1	4a	0	0	0	4.2(4)	0.416(8)
B2	4c	0.25	0.25	0.25	4.2(4)	0.506(7)
S2	4c	0.25	0.25	0.25	4.2(4)	0.494(7)
P1	4b	0.5	0.5	0.5	3.6(6)	1
S3	16e	0.6200(7)	0.6200(7)	0.6200(7)	3.6(6)	1
H1	16e	0.0761(1)	0.0761(1)	−0.0761(1)	1	0.584(8)
H2	16e	0.1739(1)	0.1739(1)	0.1739(1)	1	0.506(7)

Space group, F-43 m; lattice parameter, a = 10.0112(7) Å; R factor, Rwp = 7.63%.

a CPE. In the $Li_{5.91}PS_{4.91}(BH_4)_{1.09}$ sample, the response of the CPE/resistor has shifted to frequencies that are too high to measure with the impedance analyzer, and only the tail of the blocking electrode was used for the fit. The EIS results indicate a room-temperature (RT) ionic conductivity of 4.8 mS/cm. This value is several orders of magnitude higher than that of the precursor β-Li_3PS_4 and $LiBH_4$ (Figure S2), ensuring that we did not measure the conductivity of the remaining β-Li_3PS_4 and $LiBH_4$ precursors. The EIS spectra of $Li_{5.91}PS_{4.91}(BH_4)_{1.09}$ at different temperatures are plotted in Figure 3B. The Arrhenius plots of the BH_4-substituted Li argyrodite ($Li_{5.91}PS_{4.91}(BH_4)_{1.09}$) and conventional halogen-containing Li argyrodite (Li_6PS_5Cl and Li_6PS_5Br) are compared in Figure 3C. The RT ionic conductivity of the BH_4-substituted Li argyrodite is ~5 times higher than that of Li_6PS_5Cl (0.95 mS/cm) and Li_6PS_5Br (0.87 mS/cm) and has a lower activation energy of 0.27 eV. The Li concentration of BH_4-substituted Li argyrodite is only slightly (1.5%) lower than that of halogen-substituted argyrodites (Li_6PS_5Cl and Li_6PS_5Br), which cannot be responsible for the ~5-fold increase in ionic conductivity.[39] This result strengthens our argument that pseudohalogen substitution indeed improves the ionic conductivity of argyrodite-like compounds. To further evaluate the electrochemical performance of the BH_4-substituted Li argyrodite, a prototype all-solid-state cell was assembled with as-synthesized $Li_{5.91}PS_{4.91}(BH_4)_{1.09}$, an indium-metal anode, and a $LiNi_{0.5}Co_{0.2}Mn_{0.3}O_2$ cathode. On the cathode side, $LiNi_{0.5}Co_{0.2}Mn_{0.3}O_2$ was coated with lithium borate $Li_3B_{11}O_{18}$, which has been reported to protect the cathode from reaction with a sulfide electrolyte.[40] The cell was cycled between 1.4 and 3.7 V (2.0 and 4.3 V versus Li/Li$^+$) at a current density of 0.05 mA/cm^2 at RT. The cell was held at 3.7 V for 3 h after charging. The first-cycle capacity loss of ~60 mAh/g is likely attributable to the decomposition of the solid electrolyte. As is common in sulfides,[41] the excess charge capacity disappeared after the first cycle, indicating that a passivation layer may have formed at the interface between the electrolyte and the carbon framework. A reversible capacity of ~130 mAh/g was obtained during the first two cycles (shown in Figure 3D). However, the capacity of this all-solid-state cell faded to 101 mAh/g after 10 cycles (as shown in Figures 3D and S3), which may be attributed to the fact that a BH_4 group can be easily oxidized at high voltage.

DISCUSSION

AIMD can be an effective approach to understand how different local structures contribute to overall conductivity, as it can probe the correlation between local Li hopping and polyanion dynamics. The AIMD trajectory in a period of 10 ps at 600 K was selected to visualize the correlation between Li diffusion and polyanion

Please cite this article in press as: Sun et al., Enhanced ionic conductivity and lack of paddle-wheel effect in pseudohalogen-substituted Li argyrodites, Matter (2022), https://doi.org/10.1016/j.matt.2022.08.029

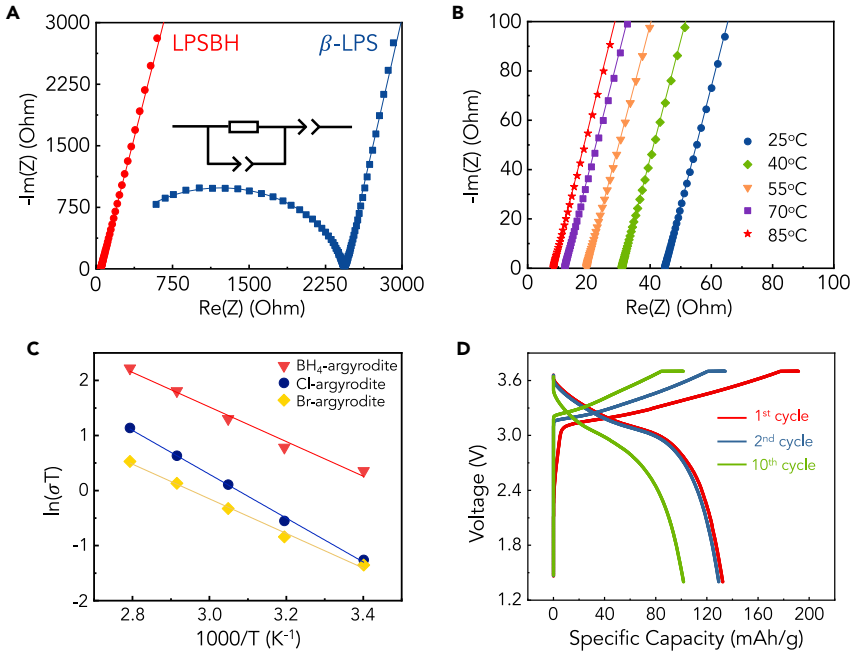

Figure 3. Electrochemical performance of BH_4-argyrodite

(A) EIS plots of $Li_{5.91}PS_{4.91}(BH_4)_{1.09}$ (LPSBH, red points) and β-Li_3PS_4 (β-LPS, blue points) at RT.

(B) EIS plots of $Li_{5.91}PS_{4.91}(BH_4)_{1.09}$ at 25°C (blue circle), 40°C (green rhombus), 55°C (orange triangle), 70°C (purple square), and 85°C (red star).

(C) Arrhenius plots of $Li_{5.91}PS_{4.91}(BH_4)_{1.09}$ (red triangle), Li_6PS_5Cl (blue sphere), and Li_6PS_5Br (yellow rhombus).

(D) Electrochemical charge and discharge of (+) $LiNi_{0.5}Co_{0.2}Mn_{0.3}O_2|Li_{5.91}PS_{4.91}(BH_4)_{1.09}|In$ (−) all-solid-state battery between 1.4 and 3.7 V at a current density of 0.05 mA/cm^2. The cell was held at 3.7 V for 3 h after charging. See also Figure S3.

groups. The atomic trajectories of selected Li with one of its first neighboring BH_4 groups and PS_4 groups are illustrated in Figures 4A and 4B. In addition to the Li migration observed in the trajectories, there is very significant BH_4 motion, such that the BH_4 trajectory almost fills the spherical space around it, as shown in Figure 4A. In contrast, because there is relatively less movement in the PS_4 group, its trajectory remains a tetrahedron shape, as observed in Figure 4B for the PS_4 group. The structural dynamics of BH_4^- and PS_4^{3-} groups predicted by AIMD are consistent with Raman spectroscopy observations. Figure 2E shows that the BH_4^- characteristic stretching modes in the BH_4 argyrodite sample are significantly broadened, in contrast to the sharp and well-resolved modes in the $LiBH_4$ lattice. This marked increase in the linewidth indicates significant damping and frequent scattering in the vibrational trajectories of the BH_4^- group in BH_4 argyrodite, which supports the AIMD result. On the other hand, as shown in Figure 2D, the PS_4^{3-} group characteristic mode at ~420 cm^{-1} largely maintains its narrow linewidth across the β-Li_3PS_4, Cl argyrodite, and BH_4 argyrodite. This behavior is consistent with the AIMD simulations showing well-defined small-amplitude vibrational motion of the PS_4^{3-} group. These observations indicate that BH_4 is very flexible and free to move locally, in contrast to PS_4. That suggests the possibility that BH_4 may easily relax away when Li moves, thereby facilitating its hopping.

Given that BH_4 and PS_4 behave quite differently in terms of vibrational motion, one may expect that the BH_4 motion will facilitate the diffusion of nearby Li. To investigate this possibility, we performed AIMD at 600 K for 10 ps and measured how long Li^+ stays

Please cite this article in press as: Sun et al., Enhanced ionic conductivity and lack of paddle-wheel effect in pseudohalogen-substituted Li argyrodites, Matter (2022), https://doi.org/10.1016/j.matt.2022.08.029

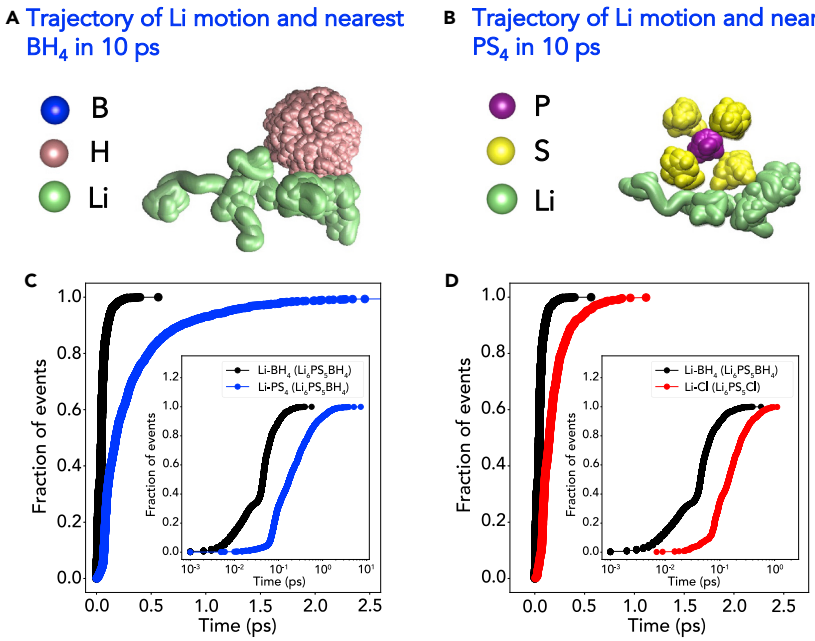

Figure 4. AIMD simulation of $Li_6PS_5BH_4$ and Li_6PS_5Cl

(A) Trajectories of one selected Li atom with its neighboring BH_4 (B is buried within the spherical trajectory of H) polyanion.

(B) Trajectories of one selected Li atom with its neighboring PS_4 polyanion.

(C) Fraction of events occurring around BH_4 and PS_4 in $Li_6PS_5BH_4$ during a simulation time of 10 ps at 600 K (semilogarithmic plot in the set). An event is defined as a Li atom entering a sphere of radius r_{Li-H} = 2.2 Å and r_{Li-S} = 2.8 Å. See also Figure S4.

(D) Fraction of events occurring around BH_4 in $Li_6PS_5BH_4$ and Cl in Li_6PS_5Cl during a simulation time of 10 ps at 600 K (semilogarithmic plot in the set). An event is defined as a Li atom entering a sphere of radius r_{Li-H} = 2.2 Å and r_{Li-Cl} = 2.8 Å.

close to a specific BH_4^- or PS_4^{3-} group once it has entered its environment. We define such an "interaction event" as occurring when Li^+ comes within a distance that is set as the maximum of the first neighbor bond length observed in the DFT relaxed structure, which is 2.2 Å for Li–H and 2.8 Å for Li–S. We have also tested our analysis with the Li–H cutoff distance being 2.8 Å while fixing the Li–S cutoff at 2.8 Å. As indicated in Figure S4, the conclusion that Li is less anchored by H still remains. Figure 4C shows the "escape curve" for both environments. More specifically, what is shown is the fraction of Li^+ in an interaction event (y axis) that has left again after a certain time (x axis). It is clear that Li^+ leaves the BH_4 environment very quickly (black curve in Figure 4C) compared with the PS_4 environment, where the Li^+ residence time is much longer (blue curves). A similar comparison is made between the Li–BH_4 residence time in $Li_6PS_5BH_4$ and the Li–Cl residence time in Li_6PS_5Cl in Figure 4D. For Li_6PS_5Cl, the interaction event radius was set as the maximum bond length of Li–Cl (2.8 Å).

As can be inferred from Figure 4C, Li^+ is much more strongly anchored near the PS_4^{3-} group than near the BH_4^- group. Almost all interaction events around BH_4 last less than 0.1 ps, whereas more than 40% of the events associated with the PS_4 group last longer than 0.1 ps. Moreover, ~10% of the Li^+ entering the PS_4 environment persists for longer than 1 ps, which is one order of magnitude longer than the longest period of events around BH_4. It is also worth mentioning that such event duration of ~0.1–1 ps is roughly the same timescale of Li hopping, as observed in the Li hopping analysis in Figure S5.

Since the PS_4 group has a larger negative charge than BH_4, one may suspect that electrostatics plays a dominant role in the anchoring of Li near PS_4. But this is inconsistent with the data in Figure 4D, which show that, even though Li–Cl interaction events in Li_6PS_5Cl have short residence times (more than 90% of the lithium escapes from the Cl^- environment occur in less than 0.25 ps), they are still substantially longer than the Li–BH_4 residence times, consistent with the increased ionic conductivity of BH_4-substituted argyrodite relative to that of Li_6PS_5Cl. It is also worth clarifying that the size of the BH_4^- cluster ion is similar to that of Cl^-, because the Li–B bond lengths in $Li_6PS_5BH_4$ are similar to the Li–Cl bond lengths in Li_6PS_5Cl (both range between 2.5 and 2.7 Å). Therefore, the enhancement of conductivity does not originate from the size difference between BH_4^- and Cl^-.

Our *ab initio* analysis clearly indicates that BH_4^- anchors the Li ions much less than PS_4^{3-} or Cl^- in argyrodites. This weakened anchoring effect and consequently higher conductivity can have two possible origins: (1) a potential dynamic coupling between Li diffusion and BH_4^- rigid rotation that facilitates Li conduction by lowering the activation barrier (also called the paddle-wheel mechanism) or (2) a weaker interaction between Li–BH_4 that flattens the Li site energy landscape near BH_4^-, which facilitates the Li motion. Mechanism (1) has been frequently mentioned in recent papers as being responsible for fast Li conduction,[18,19,30,32] whereas the role of mechanism (2) in contributing to the high conductivity has not been specifically evaluated. To determine whether one or both of these mechanisms contribute to the conductivity, we performed multiple analyses, as shown in Figure 5. In Figures 5A–5D we quantify the dynamic correlation of Li diffusion and multiple motion degrees of freedom in a BH_4 unit, whereas in Figure 5E we quantify the local electronic interaction among Li–BH_4, Li–PS_4, and Li–Cl.

In principle, the BH_4 cluster ion has 15 degrees of freedom, as each of the atoms can displace in three dimensions. To facilitate the analysis of a possible dynamic correlation, two key modes of motion of BH_4 are considered: the stretching mode and the bending mode. The translational mode of BH_4 as a unit is not considered here, since the motions that we investigate are relative to the B atom, which is also the center of mass of BH_4. The translational motion of BH_4 is captured in the motion of the Li atom relative to the B atom. As shown in Figure 5A, the first mode represents the stretching of the B–H bond, whereas the second mode reflects the bending of the B–H bond, which can lead to the rotation of H relative to B.

To quantify whether BH_4 rotates as a rigid body, we investigated the correlation between the angular changes of the B–H bonds, which should be pronounced if the BH_4 cluster rotates as a rigid body. However, our dynamic correlation analysis among the motion of the four B–H bond angles shows very little correlation (Pearson correlation analysis at Table S2 and Figure S8). Such observation indicates that the BH_4 unit does not rotate as a rigid body.

To quantify whether the Li motion is correlated with individual B–H bond motions, i.e., B–H bond stretching and B–H bond bending, the correlation between the B–H bond motion and the Li position was calculated based on event analysis similar to the one used to generate Figure 4. We collected all the partial trajectories for which Li stays in a sphere within a cutoff distance of 3.0 Å from the B atom as events to investigate a possible correlation between Li motion and B–H bond motion. If the Li motion is correlated to B–H bond motion, it should show up in the Pearson correlation of trajectories. In atomic trajectories of 10 ps of AIMD simulations at 600 K, we tracked all the "events" for which Li is close enough to a BH_4 unit. For each of the

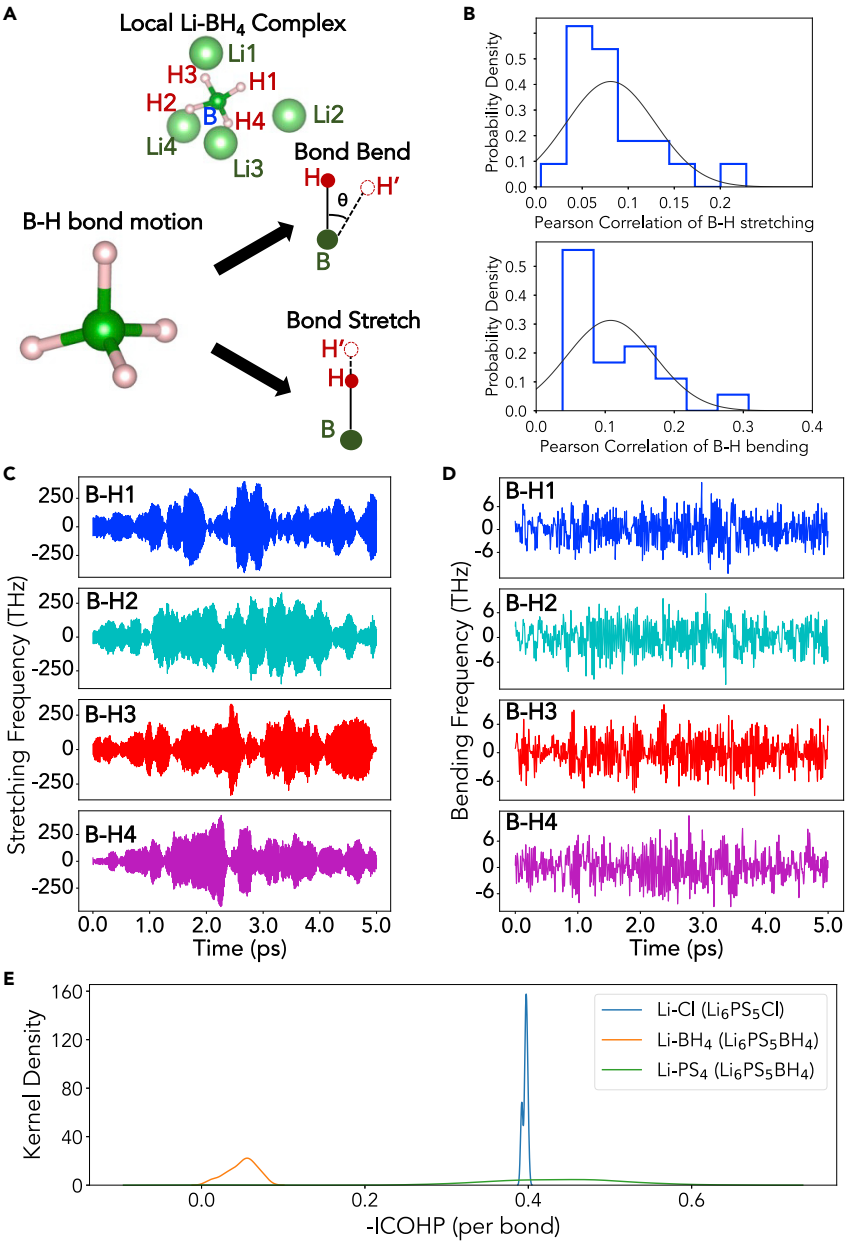

Figure 5. Correlation analyses between BH_4 and Li

(A) Demonstration of the relationship between B–H bond motion and Li diffusion. The motion of the B–H bond can be decomposed into stretching and bending modes.

(B) Probability distribution of the Pearson correlation between the stretching of the B–H bond and the Li motion as well as the probability distribution of the Pearson correlation between the bending of the B–H bond and the Li motion.

(C) Demonstration of the calculated frequency evolution of the B–H bond-stretching degree of freedom as a function of time for a selected BH_4 unit as shown in (A).

(D) Demonstration of the calculated frequency evolution of the B–H bond-bending degree of freedom as a function of time for a selected BH_4 unit as shown in (A). See also Figure S6.

(E) Kernel density distribution of calculation −ICOHP value of Li–Cl, Li–BH_4, and Li–PS_4 bonding in Li_6PS_5Cl and $Li_6PS_5BH_4$.

events, we obtained a time series of the Li–B and B–H displacement. We could then calculate and average the Pearson correlation coefficient of these two displacements with either stretching or bending. Both the histogram and the estimated kernel density of the probability distribution of the average correlation of all the Li atoms are shown in Figure 5B.

For B–H bond stretching, we checked the correlation between changes in the B–H bond length and the Li–B distance. The Pearson coefficient,[42] in this case, is defined as:

$$Corr = \frac{cov(l_{B-H}(t), l_{Li-B}(t))}{\sigma(l_{B-H}(t))\sigma(l_{Li-B}(t))}, \quad \text{(Equation 1)}$$

where $l_{B-H}(t)$ refers to the stretching length of the B–H bond, $l_{Li-B}(t)$ refers to the Li–B distance in the defined event, $cov(l_{B-H}(t),\ l_{Li-B}(t))$ refers to the covariance of Li–B distance and the stretching length of the B–H bond, while $\sigma(l_{B-H}(t))$ and $\sigma(l_{Li-B}(t))$ are the standard deviation of the Li–B distance and the stretching length of the B–H bond. For B–H bond bending, we evaluated the correlation between the B–H bending angle $\theta_{B-H}(t)$ and the Li–B bending angle $\theta_{Li-B}(t)$. We used Li–B bending angle as an indication of the motion of Li with respect to the corresponding B–H bond because the displacement of the Li atom itself does not give the relative position information of Li with respect to the B–H bond. The intercorrelation between these two bending angles can then be quantified using the Pearson correlation coefficient:

$$Corr = \frac{cov(\theta_{B-H}(t), \theta_{Li-B}(t))}{\sigma(\theta_{B-H}(t))\sigma(\theta_{Li-B}(t))}. \quad \text{(Equation 2)}$$

In Equation (2), $cov(\theta_{B-H}(t),\ \theta_{Li-B}(t))$ refers to the covariance of two bending angles, while $\sigma(\theta_{B-H}(t))$ and $\sigma(\theta_{Li-B}(t))$ are the standard deviation of the bending angles.

It can be clearly inferred from Figure 5B that neither the B–H bond stretching nor the bond bending is particularly correlated to the motion of Li atoms nearby. The maximum correlation coefficient observed is less than 0.2, and most of the coefficients are smaller than 0.1. Given that a correlation smaller than 0.5 is generally regarded as weak in statistics,[43,44] the calculated value indicates that even though the B–H bond bends and stretches very fast, the position of Li is not correlated to the movement of B–H bonds. Considering that rigid rotation of the BH_4 unit is absent, and the movement of individual B–H bond shows little correlation with Li diffusion, there is no evidence to conclude that the enhanced conductivity in this material originates from a paddle-wheel mechanism.

To further corroborate the origin of the weak correlation between BH_4 motion and Li diffusion, we calculated the frequencies of the stretching and bending degrees of freedom for the B–H bond, as shown in Figures 5C and 5D. For stretching degree of freedom, the frequency can be estimated as:

$$f_{stretching} = \frac{1}{l_{max}} \times \frac{d(l_{B-H})}{dt}. \quad \text{(Equation 3)}$$

Here, l_{max} refers to the maximum amplitude of bond stretching as observed in the period of 10 ps. For bending degree of freedom, the frequency can be estimated as:

$$f_{bending} = \frac{1}{360^0} \times \frac{d(\theta_{B-H})}{dt}. \quad \text{(Equation 4)}$$

Please cite this article in press as: Sun et al., Enhanced ionic conductivity and lack of paddle-wheel effect in pseudohalogen-substituted Li argyrodites, Matter (2022), https://doi.org/10.1016/j.matt.2022.08.029

The evolution of the frequencies of stretching and bending degrees of freedom is demonstrated in Figures 5C and 5D. Since the frequency at each time frame is calculated from the first derivative of the velocities, the overall analysis will not be significantly modified by longer trajectories. We have also confirmed this by plotting the frequency evolution over the shorter time of 1 ps (Figure S6). As indicated in Figure 5C, the stretching frequency has a magnitude ranging from a few tens of terahertz to 200 THz, while the bending frequency in Figure 5D has a magnitude of several terahertz, which is consistent with observations on BH_4 groups in $Mg(BH)_4$.[45] Given that the Li hopping frequency is calculated to be well below 1 THz (Figure S5), it turns out that both B–H bond stretching and B–H bond bending occur at a higher-frequency time frame than the Li hops, so that B–H bond motion and Li motion can be decoupled.

Finally, to verify whether the weaker anchoring effect of BH_4^- on Li^+ is related to weak electronic interaction between Li^+ and BH_4^-, we calculated the integrated crystal orbital Hamilton population (−ICOHP) to quantify the chemical bonding strength of Li–BH_4, Li–PS_4, and Li–Cl (Figure 5E).[46,47] As shown in Figure 5E, the −ICOHP value of the Li–BH_4 bond is much smaller than that of the Li–PS_4 bond or Li–Cl bond, which reveals significantly weaker electronic interaction. Therefore, we confirmed that the enhanced ionic conductivity has little to do with a dynamic correlation among Li diffusion and B–H bond motion (e.g., the paddle-wheel mechanism), but is mostly caused by weak electronic interaction between the Li^+ and the BH_4^- group. It should also be noted that the influence of weak electronic interaction between Li and the anion framework on Li ionic conduction has also been discussed in the context of the inductive effect that central ions in MS_4 tetrahedra have on the Li conduction in $Li_{10}GeP_2S_{12}$(LGPS)-like structures.[48]

Conclusion

In this work, we investigated the Li-argyrodite system to explore the possibility of enhancing ionic conductivity through pseudohalogen substitution. *Ab initio* computational screening to predict the synthetic accessibility of Li argyrodites with different pseudohalogen substitutions suggested that, among many possible polyanions, BH_4 could most likely substitute for the S in the 4a and 4c sites in the argyrodite structure. This BH_4-substituted Li argyrodite ($Li_{5.91}PS_{4.91}(BH_4)_{1.09}$) was successfully synthesized via a mechanochemical method and shows an ionic conductivity of 4.8 mS/cm, ~5 times higher than that of common halogen-substituted Li argyrodites (Li_6PS_5Cl and Li_6PS_5Br), confirming the positive contribution of a cluster ion to the Li-ion conductivity. AIMD analysis demonstrates that the enhancement of the Li-ion conductivity originates from the weaker anchoring effect the pseudohalide anion has on Li^+. We found no evidence for any correlation between B–H bond motion and Li motion, indicating that no paddle-wheel effect is needed to explain the enhanced conductivity.

EXPERIMENTAL PROCEDURES

Resource availability

Lead contact

Further information and requests for resources and reagents should be directed to and will be fulfilled by the lead contact, Gerbrand Ceder (gceder@berkeley.edu).

Materials availability

The materials generated in this study are available from the lead contact upon request.

Please cite this article in press as: Sun et al., Enhanced ionic conductivity and lack of paddle-wheel effect in pseudohalogen-substituted Li argyrodites, Matter (2022), https://doi.org/10.1016/j.matt.2022.08.029

Data and code availability

The authors declare that the data supporting the findings of this study are available within the paper and its supplemental information files. The data and code are available from the lead contact upon reasonable request.

Synthesis

β-Li_3PS_4 was synthesized using lithium sulfide (Li_2S; Sigma-Aldrich, 99.98% trace metals basis) and phosphor sulfide (P_2S_5; Sigma-Aldrich, 99%) mixed in a 2:1 molar ratio (excess P_2S_5 was used) in acetonitrile (Sigma-Aldrich, anhydrous, 99.8%). The suspension was stirred for 24 h and filtered to obtain the precipitate. The precipitate was washed with acetonitrile (ACN) three times and dried at 80°C for 12 h to obtain Li_3PS_4 ● 2ACN. The as-obtained Li_3PS_4 ● 2ACN was then heated under vacuum at 150°C for 24 h to obtain β-Li_3PS_4. The as-synthesized β-Li_3PS_4 and $LiBH_4$ (Aldrich, >95%) were mixed in a 1:2 molar ratio and hand-ground in an agate mortar for 15 min. Then, 0.8 g of the powder mixture and 80 g of zirconium oxide balls (5 mm in diameter) were placed into a zirconium oxide ball-mill jar and ball milled (SpexSamplePrep 8000M) for 2 h. To prevent the sample temperature from becoming too high, ball milling was paused for 15 min after every 30 min milling. The mixture was further annealed at 150°C for 48 h to obtain BH_4-substitutued argyrodite. Because of the sensitivity to O_2 and moisture of the system, all the experimental procedures were performed in an argon atmosphere with <0.1 ppm of O_2 and H_2O.

Li_6PS_5X (X = Cl, Br) samples were synthesized via a previously reported method.[3] Li_2S (Sigma-Aldrich, 99.98% trace metals basis), P_2S_5 (Sigma-Aldrich, 99%), LiCl (Sigma-Aldrich, >99.98% trace metals basis), and LiBr (Sigma-Aldrich, >99%) were mixed in the appropriate stoichiometric ratio. The mixtures were hand-ground in an agate mortar for 15 min and then pressed into pellets of 6.0 mm in diameter under a pressure of 2.0 metric tons for 4 min. The pellets were then filled into quartz ampules (12 mm inner diameter and ~15 cm in length), which were sealed under vacuum. The ampules were carbon-coated and preheated to avoid traces of water. The reaction was performed at 550°C for 144 h to obtain Li_6PS_5X (X = Cl, Br).

Cl-substituted argyrodite and Br-substituted argyrodite were also prepared by the same synthesis approach as was used for the BH_4-substituted argyrodite. β-Li_3PS_4 and LiX (X = Cl, Br) were mixed in a 1:2 molar ratio and hand-ground in an agate mortar for 15 min. Then, 0.8 g of the powder mixture and 80 g of zirconium oxide balls (5 mm in diameter) were placed into a zirconium oxide ball-mill jar and ball milled (SpexSamplePrep 8000M) for 2 h. Ball milling was paused for 15 min after every 30 min milling. The mixture was further annealed at 150°C for 48 h to obtain Cl-substituted argyrodite and Br-substituted argyrodite. The EIS spectra of these halide-substituted argyrodites are shown in Figure S7.

Electrochemistry

The Li-ion conductivity was evaluated using EIS with tantalum metal as blocking electrodes at temperatures ranging from 20°C to 85°C. The solid-electrolyte powder was uniaxially compressed under a pressure of 520 MPa to make a ~1-mm-thick pellet with a diameter of 7.7 mm and then sandwiched by two tantalum foils. EIS measurements were performed using an EC-Lab Electrochemistry SP300 system (Biologic). The measurements were conducted at the initial open-circuit voltage in the frequency range of 7 MHz–10 mHz with the application of a 10-mV signal amplitude. The measurements were performed using a BioLogic controlled environment sample holder assembled and sealed in an Ar-filled glovebox.

Please cite this article in press as: Sun et al., Enhanced ionic conductivity and lack of paddle-wheel effect in pseudohalogen-substituted Li argyrodites, Matter (2022), https://doi.org/10.1016/j.matt.2022.08.029

Solid-state cells were also fabricated in an Ar-filled glovebox. The cathode composite was prepared by first hand grinding 65 mg of LBO-coated $LiNi_{0.5}Co_{0.2}Mn_{0.3}O_2$ powder (from Samsung Research Japan[40]) and 30 mg of $Li_{5.91}PS_{4.91}(BH_4)_{1.09}$ for 20 min and then grinding them for another 20 min after adding 5 mg of carbon nanofibers (CNFs; from Samsung Research Japan). The cell was assembled using a custom-made pressure cell consisting of a polyether ketone (PEEK) cylinder with an inner diameter of 8 mm and two 8-mm-diameter stainless-steel rods as current collectors. One end of the cylinder was first closed with a current collector. Then, 40 mg $Li_{5.91}PS_{4.91}(BH_4)_{1.09}$ as the electrolyte was added and compressed under a pressure of 100 MPa. Then, 5 mg of the cathode composite was spread evenly on top of the electrolyte membrane and compacted under pressure of 200 MPa. Finally, an 8-mm-diameter piece of In metal was attached on the other side of the electrolyte membrane as the anode and compacted under 200 MPa pressure again. The entire cell was sealed in an Ar-filled jar and cycled under 5 MPa stack pressure provided by a spring. Cell cycling was performed using a Bio-Logic VMP300 system.

Characterization

For structure determination, synchrotron XRD data were collected at beamline 11BM at the Advanced Photon Source at Argonne National Laboratory. Because of the air sensitivity of the sample, the $Li_{5.91}PS_{4.91}(BH_4)_{1.09}$ powder was sealed into 0.0395-in-diameter polyimide tubing in an argon glovebox. Rietveld refinement was performed using the TOPAS v.6 software package (Bruker). Chebyshev polynomials were used for the background fitting. A fundamental parameters approach was used for the peak shape modeling. The constraints for the structural factor refinement were as follows (Occ(X) represents the site occupancy of atom X at the related Wyckoff position):

(1) 4a sites are fully occupied by B1 and S1:
Occ(B1) + Occ(S1) = 1.
(2) 4c sites are fully occupied by B2 and S2:
Occ(B2) + Occ(S2) = 1.
(3) H1 is bonded to B1 and H2 is bonded to B2:
Occ(B1) = Occ(H1), Occ(B2) = Occ(H2).
(4) Based on the charge balance, we could get:
12Occ(Li1) + 6Occ(Li2) + Occ(B1) + Occ(B2) = 7.

TEM ED and EDS measurements were performed on an FEI TitanX 60–300 microscope equipped with the Bruker windowless EDS detector at an accelerating voltage of 300 kV in the Molecular Foundry at LBNL. The simulated ED ring pattern for argyrodite structure (ICDD 04-018-1429) was generated with the Single Crystal 4 diffraction simulation software. Raman spectroscopy measurements were carried out using a home-built confocal microspectroscopy setup. Briefly, a Coherent Verdi-V2 single-frequency laser was used as the excitation source at a wavelength of 532 nm. The excitation laser was focused onto the sample surface using a 60× NA0.7 Nikon ELWD objective. The same objective collected the backscattered light. The collected signals were sent through 532 nm notch filters to remove the Rayleigh line and then focused onto the entrance slit of a spectrometer. An IsoPlane 320 spectrometer equipped with a 1,800 g/mm grating was used to disperse the signal onto a PIXIS 400 thermoelectrically cooled CCD. All samples were pellets pressed in an argon-filled glovebox and sealed using PET/PE encapsulations.

Please cite this article in press as: Sun et al., Enhanced ionic conductivity and lack of paddle-wheel effect in pseudohalogen-substituted Li argyrodites, Matter (2022), https://doi.org/10.1016/j.matt.2022.08.029

Computational methods

DFT structural optimization and total energy calculations

Because of the partial occupancy of Li sites in the argyrodite structure, structural enumerations in a supercell with only 48h Li sites were performed, and first-principle calculations were performed on the top 10 structures with lowest electrostatic energy using DFT as implemented in the plane-wave-basis-set Vienna *ab initio* simulation package (VASP). The structure with the lowest DFT energy was then selected for further AIMD simulation. Projector augmented wave potentials with a kinetic energy cutoff of 520 eV were used in all the structural optimizations and total-energy calculations, and the exchange and correlation functionals were described within the Perdew-Burke-Ernzerhof generalized gradient approximation (GGA-PBE). The k-point grid in each dimension was set as 25 Å divided by the exact length of that dimension.

Phase stability analysis

The thermodynamic stability was evaluated using the calculated DFT total energy. The stability of any phase was evaluated by comparing its energy with linear combinations of the energy of other phases (leading to the same composition) using the convex-hull construction. The stability analysis was performed versus all the compounds in our internal database, which includes both phases from the Inorganic Crystal Structure Database (ICSD: http://icsd.fiz-karlsruhe.de/icsd/) and some compounds generated from data-mined substitution rules.[49] The phase stability was quantified by evaluating the E_{hull}, which refers to the compound decomposition energy to materials at the hull. A non-negative value of the E_{hull} energy indicates a thermodynamic driving force for decomposition into alternate phases. To correct the overestimation of the binding energy by the GGA-PBE functional, we followed previous approaches[50,51] to apply constant energy corrections of −0.66 eV per S atom. On the basis of the DFT calculated charge density and wave function, we performed COHP analysis using the LOBSTER package.[46,47]

Li-ion diffusivity and conductivity calculations

AIMD simulation was used to investigate the ionic conductivity of Li ions. For all the AIMD calculations, an NVT ensemble was applied with a time step of 1 fs and a Nosé-Hoover thermostat[52] with a period of 100 fs. A minimal Γ-point-only grid was used with spin-polarized calculations. The AIMD simulations were run at 600 K, 700 K, 800 K, and 1000 K. All the data were fitted assuming Arrhenius behavior to obtain the activation energy, diffusion prefactor, and RT diffusivity. The lowest-energy atomic configurations were used as the initial configuration of the AIMD simulations.

SUPPLEMENTAL INFORMATION

Supplemental information can be found online at https://doi.org/10.1016/j.matt.2022.08.029.

ACKNOWLEDGMENTS

This work was supported by the Assistant Secretary for Energy Efficiency and Renewable Energy, Vehicle Technologies Office of the US Department of Energy under contract no. DE-AC02-05CH11231, under the Advanced Battery Materials Research (BMR) Program. The computational analysis was performed using computational resources sponsored by the Department of Energy's Office of Energy Efficiency and Renewable Energy and located at the National Renewable Energy Laboratory; computational resources provided by the Extreme Science and Engineering

Discovery Environment (XSEDE), supported by National Science Foundation grant ACI1053575; as well as the National Energy Research Scientific Computing Center (NERSC), a DOE Office of Science User Facility supported by the Office of Science and the US Department of Energy under contract DE-AC02-05CH11231. Work at the Molecular Foundry was supported by the Office of Science, Office of Basic Energy Sciences, of the US Department of Energy under Contract DE-AC02-05CH11231. Raman spectroscopy and analysis were supported by the National Science Foundation/EPSCoR RII Track-1: Emergent Quantum Materials and Technologies (EQUATE), Award OIA-2044049.

AUTHOR CONTRIBUTIONS

Conceptualization, Y.S., B.O., and G.C.; methodology, Y.S. and B.O.; formal analysis, Y.S., B.O., Y.W., Z.C., and V.L.; investigation, Y.S., B.O., Y.Z., S.S., and Y.G.; resources, Y.Z., S.S., and Y.G.; writing – original draft, Y.S., B.O., and G.C.; writing – review & editing, Y.S., B.O., and G.C.; funding acquisition, Y.G. and G.C.; supervision, G.C.

DECLARATION OF INTERESTS

The authors declare no competing interests.

Received: February 22, 2022
Revised: July 27, 2022
Accepted: August 30, 2022
Published: September 27, 2022

REFERENCES

1. Motavalli, J. (2015). Technology: a solid future. Nature *526*, S96–S97. https://doi.org/10.1038/526S96a.

2. Ceder, G., Ong, S.P., and Wang, Y. (2018). Predictive modeling and design rules for solid electrolytes. MRS Bull. *43*, 746–751. https://doi.org/10.1557/mrs.2018.210.

3. Deiseroth, H.J., Kong, S.T., Eckert, H., Vannahme, J., Reiner, C., Zaiss, T., and Schlosser, M. (2008). Li6PS5X: a class of crystalline Li-rich solids with an unusually high Li+ mobility. Angew. Chem. Int. Ed. Engl. *47*, 755–758. https://doi.org/10.1002/anie.200703900.

4. Adeli, P., Bazak, J.D., Park, K.H., Kochetkov, I., Huq, A., Goward, G.R., and Nazar, L.F. (2019). Boosting solid-state diffusivity and conductivity in lithium superionic argyrodites by halide substitution. Angew. Chem. Int. Ed. Engl. *131*, 8773–8778. https://doi.org/10.1002/ANGE.201814222.

5. Richards, W.D., Wang, Yan, Miara, L.J., Kim, J.C., Ceder, G., and Ceder, Gerbrand (2016). Design of Li 1+2x Zn 1−x PS 4 , a new lithium ion conductor. Energy Environ. Sci. *9*, 3272–3278. https://doi.org/10.1039/C6EE02094A.

6. Murugan, R., Thangadurai, V., and Weppner, W. (2007). Fast lithium ion conduction in garnet-type Li7La 3Zr2O12. Angew. Chem. Int. Ed. Engl. *46*, 7778–7781. https://doi.org/10.1002/anie.200701144.

7. Bo, Shou-Hang, Wang, Yan, and Ceder, Gerbrand (2016). Structural and Na-ion conduction characteristics of Na 3 PS x Se 4−x. J. Mater. Chem. A. *4*, 9044–9053. https://doi.org/10.1039/C6TA03027K.

8. Wang, Y., Richards, W.D., Ong, S.P., Miara, L.J., Kim, J.C., Mo, Y., and Ceder, G. (2015). Design principles for solid-state lithium superionic conductors. Nat. Mater. *14*, 1026–1031. https://doi.org/10.1038/nmat4369.

9. Xiao, Y., Jun, K., Wang, Y., Miara, L.J., Tu, Q., and Ceder, G. (2021). Lithium oxide superionic conductors inspired by garnet and NASICON structures. Adv. Energy Mater. *11*, 2101437. https://doi.org/10.1002/AENM.202101437.

10. Richards, W.D., Wang, Y., Miara, L.J., Kim, J.C., and Ceder, G. (2016). Design of Li 1+2x Zn 1−x PS 4 , a new lithium ion conductor. Energy Environ. Sci. *9*, 3272–3278. https://doi.org/10.1039/C6EE02094A.

11. Liu, Y., Wang, S., Nolan, A.M., Ling, C., Mo, Y., Li, garnet, Li, N., Liu, Y., Wang, S., Nolan, A.M., et al. (2020). Tailoring the cation lattice for chloride lithium-ion conductors. Adv. Energy Mater. *10*, 2002356. https://doi.org/10.1002/AENM.202002356.

12. Wang, R., Ping, W., Wang, C., Liu, Y., Gao, J., Dong, Q., Wang, X., Mo, Y., Hu, L., Wang, R., et al. (2020). Computation-guided synthesis of new garnet-type solid-state electrolytes via an ultrafast sintering technique. Adv. Mater. *32*, 2005059. https://doi.org/10.1002/ADMA.202005059.

13. Canepa, P., Bo, S.H., Sai Gautam, G., Key, B., Richards, W.D., Shi, T., Tian, Y., Wang, Y., Li, J., and Ceder, G. (2017). High magnesium mobility in ternary spinel chalcogenides. Nat. Commun. *8*, 1759–1768. https://doi.org/10.1038/s41467-017-01772-1.

14. Matsuo, M., and Orimo, S.I. (2011). Lithium fast-ionic conduction in complex hydrides: review and prospects. Adv. Energy Mater. *1*, 161–172. https://doi.org/10.1002/AENM.201000012.

15. Unemoto, A., Wu, H., Udovic, T.J., Matsuo, M., Ikeshoji, T., and Orimo, S.I. (2016). Fast lithium-ionic conduction in a new complex hydride-sulphide crystalline phase. Chem. Commun. *52*, 564–566. https://doi.org/10.1039/c5cc07793a.

16. Wang, F., Evans, H.A., Kim, K., Yin, L., Li, Y., Tsai, P.-C., Liu, J., Lapidus, S.H., Brown, C.M., Siegel, D.J., and Chiang, Y.M. (2020). Dynamics of hydroxyl anions promotes lithium ion conduction in antiperovskite Li2OHCl. Chem. Mater. *32*, 8481–8491. https://doi.org/10.1021/ACS.CHEMMATER.0C02602.

17. Fang, H., and Jena, P. (2017). Li-rich antiperovskite superionic conductors based on cluster ions. Proc. Natl. Acad. Sci. USA. *114*, 11046–11051. https://doi.org/10.1073/PNAS.1704086114.

18. Fang, H., and Jena, P. (2018). Sodium superionic conductors based on clusters. ACS Appl. Mater. Inter. *11*, 963–972. https://doi.org/10.1021/ACSAMI.8B19003.

19. Sun, Y., Wang, Y., Liang, X., Xia, Y., Peng, L., Jia, H., Li, H., Bai, L., Feng, J., Jiang, H., and Xie, J. (2019). Rotational cluster Anion enabling superionic conductivity in sodium-rich antiperovskite Na3OBH4. J. Am. Chem. Soc. *141*, 5640–5644. https://doi.org/10.1021/JACS.9B01746.

20. Zhou, L., Assoud, A., Zhang, Q., Wu, X., and Nazar, L.F. (2019). New family of argyrodite thioantimonate lithium superionic conductors. J. Am. Chem. Soc. *141*, 19002–19013. https://doi.org/10.1021/JACS.9B08357.

21. Zhou, L., Minafra, N., Zeier, W.G., and Nazar, L.F. (2021). Innovative approaches to Li-argyrodite solid electrolytes for all-solid-state lithium batteries. Acc. Chem. Res. *54*, 2717–2728. https://doi.org/10.1021/ACS.ACCOUNTS.0C00874.

22. Zhou, L., Park, K.H., Sun, X., Lalère, F., Adermann, T., Hartmann, P., and Nazar, L.F. (2019). Solvent-engineered design of argyrodite Li6PS5X (X = Cl, Br, I) solid electrolytes with high ionic conductivity. ACS Energy Lett. *4*, 265–270. https://doi.org/10.1021/acsenergylett.8b01997.

23. Kaup, K., Bishop, K., Assoud, A., Liu, J., and Nazar, L.F. (2021). Fast ion-conducting thioboracite with a perovskite topology and argyrodite-like lithium substructure. J. Am. Chem. Soc. *143*, 6952–6961. https://doi.org/10.1021/JACS.1C00941.

24. Ouyang, B., Wang, Y., Sun, Y., and Ceder, G. (2020). Computational investigation of halogen-substituted Na argyrodites as solid-state superionic conductors. Chem. Mater. *32*, 1896–1903. https://doi.org/10.1021/ACS.CHEMMATER.9B04541.

25. De Klerk, N.J.J., Rosłoń, I., and Wagemaker, M. (2016). Diffusion mechanism of Li argyrodite solid electrolytes for Li-ion batteries and prediction of optimized halogen doping: the effect of Li vacancies, halogens, and halogen disorder. Chem. Mater. *28*, 7955–7963. https://doi.org/10.1021/acs.chemmater.6b03630.

26. Kraft, M.A., Culver, S.P., Calderon, M., Böcher, F., Krauskopf, T., Senyshyn, A., Dietrich, C., Zevalkink, A., Janek, J., and Zeier, W.G. (2017). Influence of lattice polarizability on the ionic conductivity in the lithium superionic argyrodites Li6PS5X (X = Cl, Br, I). J. Am. Chem. Soc. *139*, 10909–10918. https://doi.org/10.1021/jacs.7b06327.

27. Patel, S.V., Banerjee, S., Liu, H., Wang, P., Chien, P.H., Feng, X., Liu, J., Ong, S.P., and Hu, Y.Y. (2021). Tunable lithium-ion transport in mixed-halide argyrodites Li6- xPS5- xClBrx: an unusual compositional space. Chem. Mater. *33*, 1435–1443. https://doi.org/10.1021/ACS.CHEMMATER.0C04650.

28. Feng, X., Chien, P.H., Wang, Y., Patel, S., Wang, P., Liu, H., Immediato-Scuotto, M., and Hu, Y.Y. (2020). Enhanced ion conduction by enforcing structural disorder in Li-deficient argyrodites Li6−xPS5−xCl1+x. Energy Storage Mater. *30*, 67–73. https://doi.org/10.1016/J.ENSM.2020.04.042.

29. Wang, P., Liu, H., Patel, S., Feng, X., Chien, P.H., Wang, Y., and Hu, Y.Y. (2020). Fast ion conduction and its origin in Li6- xPS5- xBr1+ x. Chem. Mater. *32*, 3833–3840. https://doi.org/10.1021/ACS.CHEMMATER.9B05331.

30. Smith, J.G., and Siegel, D.J. (2020). Low-temperature paddlewheel effect in glassy solid electrolytes. Nat. Commun. *11*, 1483–1511. https://doi.org/10.1038/s41467-020-15245-5.

31. Song, A., Turcheniuk, K., Leisen, J., Xiao, Y., Meda, L., Borodin, O., and Yushin, G. (2020). Understanding Li-ion dynamics in lithium hydroxychloride (Li2OHCl) solid state electrolyte via addressing the role of protons. Adv. Energy Mater. *10*, 1903480. https://doi.org/10.1002/AENM.201903480.

32. Zhang, Z., Roy, P.-N., Li, H., Avdeev, M., and Nazar, L.F. (2019). Coupled cation–anion dynamics enhances cation mobility in room-temperature superionic solid-state electrolytes. J. Am. Chem. Soc. *141*, 19360–19372. https://doi.org/10.1021/JACS.9B09343.

33. Ong, S.P., Wang, L., Kang, B., and Ceder, G. (2008). Li−Fe−P−O2 phase diagram from first principles calculations. Chem. Mater. *20*, 1798–1807. https://doi.org/10.1021/CM702327G.

34. Ong, S.P., Mo, Y., Richards, W.D., Miara, L., Lee, H.S., and Ceder, G. (2013). Phase stability, electrochemical stability and ionic conductivity of the Li 10±1 MP 2 X 12 (M = Ge, Si, Sn, Al or P, and X = O, S or Se) family of superionic conductors. Energy Environ. Sci. *6*, 148–156. https://doi.org/10.1039/C2EE23355J.

35. Mo, Y., Ong, S.P., and Ceder, G. (2012). First principles study of the Li 10GeP 2S 12 lithium super ionic conductor material. Chem. Mater. *24*, 15–17. https://doi.org/10.1021/CM203303Y.

36. Sun, W., Dacek, S.T., Ong, S.P., Hautier, G., Jain, A., Richards, W.D., Gamst, A.C., Persson, K.A., and Ceder, G. (2016). The thermodynamic scale of inorganic crystalline metastability. Sci. Adv. *2*, e1600225. https://doi.org/10.1126/sciadv.1600225.

37. Sakuda, A., Yamauchi, A., Yubuchi, S., Kitamura, N., Idemoto, Y., Hayashi, A., and Tatsumisago, M. (2018). Mechanochemically prepared Li2S–P2S5–LiBH4 solid electrolytes with an argyrodite structure. ACS Omega *3*, 5453–5458. https://doi.org/10.1021/ACSOMEGA.8B00377.

38. Züttel, A., Wenger, P., Rentsch, S., Sudan, P., Mauron, P., and Emmenegger, C. (2003). LiBH4 a new hydrogen storage material. J. Power Sourc. *118*, 1–7. https://doi.org/10.1016/S0378-7753(03)00054-5.

39. Wu, L., Zhang, Z., Liu, G., Weng, W., Zhang, Z., and Yao, X. (2021). Wet-milling synthesis of superionic lithium argyrodite electrolytes with different concentrations of lithium vacancy. ACS Appl. Mater. Inter. *13*, 46644–46649. https://doi.org/10.1021/ACSAMI.1C13031.

40. Zhang, Y.-Q., Tian, Y., Xiao, Y., Miara, L.J., Aihara, Y., Tsujimura, T., Shi, T., Scott, M.C., and Ceder, G. (1903). Direct visualization of the interfacial degradation of cathode coatings in solid state batteries: a combined experimental and computational study. Adv. Energy Mater. https://doi.org/10.1002/aenm.201903778.

41. Tian, Y., Shi, T., Richards, W.D., Li, J., Kim, J.C., Bo, S.-H., and Ceder, G. (2017). Compatibility issues between electrodes and electrolytes in solid-state batteries. Energy Environ. Sci. *10*, 1150–1166. https://doi.org/10.1039/C7EE00534B.

42. Soper, H.E., Young, A.W., Cave, B.M., Lee, A., and Pearson, K. (1917). On the distribution of the correlation coefficient in small samples. Appendix II to the papers of "student" and R. A. Fisher. Biometrika *11*, 328. https://doi.org/10.2307/2331830.

43. Rodgers, J.L., Nicewander, W.A., and Alan, W. (1988). Thirteen ways to look at the correlation coefficient. Am. Stat. *42*, 59–66.

44. Buda, A., and Jarynowski, A. (2010). Life Time of Correlations and its Applications (Andrzej Buda Wydawnictwo NiezaleĹĽne).

45. George, L., Drozd, V., Saxena, S.K., Bardaji, E.G., and Fichtner, M. (2009). Structural phase transitions of Mg(BH4)2 under pressure. J. Phys. Chem. C *113*, 486–492. https://doi.org/10.1021/JP807842T.

46. Dronskowski, R., and Bloechl, P.E. (1993). Crystal orbital Hamilton populations (COHP). Energy-resolved visualization of chemical bonding in solids based on density-functional calculations. J. Phys. Chem. *97*, 8617–8624. https://doi.org/10.1021/J100135A014.

47. Deringer, V.L., Tchougréeff, A.L., and Dronskowski, R. (2011). Crystal orbital Hamilton population (COHP) analysis as projected from plane-wave basis sets. J. Phys. Chem. A. *115*, 5461–5466. https://doi.org/10.1021/JP202489S.

48. Culver, S.P., Squires, A.G., Minafra, N., Armstrong, C.W.F., Krauskopf, T., Böcher, F., Li, C., Morgan, B.J., and Zeier, W.G. (2020). Evidence for a solid-electrolyte inductive effect in the superionic conductor Li10Ge1-xSnxP2S12. J. Am. Chem. Soc. *142*, 21210–21219. https://doi.org/10.1021/JACS.0C10735.

49. Hautier, G., Fischer, C., Ehrlacher, V., Jain, A., and Ceder, G. (2011). Data mined ionic substitutions for the discovery of new compounds. Inorg. Chem. *50*, 656–663. https://doi.org/10.1021/IC102031H.

50. Wang, L., Maxisch, T., and Ceder, G. (2006). Oxidation energies of transition metal oxides within the GGA+U framework. Phys. Rev. B *73*, 195107. https://doi.org/10.1103/PhysRevB.73.195107.

51. Wang, Y., Richards, W.D., Bo, S.-H., Miara, L.J., and Ceder, G. (2017). Computational prediction and evaluation of solid-state sodium superionic conductors Na7P3X11 (X = O, S, Se). Chem. Mater. *29*, 7475–7482. https://doi.org/10.1021/ACS.CHEMMATER.7B02476.

52. Nosé, S. (1984). A unified formulation of the constant temperature molecular dynamics methods. J. Chem. Phys. *81*, 511–519. https://doi.org/10.1063/1.447334.